Available online at www.sciencedirect.com
ScienceDirect
Journal of the European Ceramic Society 28 (2008) 2823–2834
www.elsevier.com/locate/jeurceramsoc

Fracture properties of spray-dried powder compacts: Effect of granule size

J.L. Amorós, V. Cantavella *, J.C. Jarque, C. Felíu

Instituto de Tecnología Cerámica, Asociación de Investigación de las Industrias Cerámicas, Universitat Jaume I, Castellón, Spain

Received 17 October 2007; received in revised form 5 May 2008; accepted 6 May 2008
Available online 25 June 2008

Abstract

Inappropriate mechanical properties of spray-dried powder compacts lead to significant green product losses, entailing considerable costs in ceramic tile manufacture as well as serious environmental problems. In addition, green strength can be indicative of how well a ceramic processing system is working.

In this study, granules were prepared by spray drying a red clay slurry used in floor tile manufacture. The resulting granules were characterised and their porosity, morphology, and mechanical behaviour were determined.

The study analyses the fracture properties of green ceramic materials using Linear Elastic Fracture Mechanics (LEFM), which has been widely used for fired materials, but whose application to green compacts has drawn much less attention. Two types of tests for determining fracture parameters (fracture toughness, fracture energy, and crack size) in green materials are also critically examined. Finally, the fracture parameters have been correlated to the microstructural characteristics of the compacts, in particular to granule size and the topography of the fracture.

Keywords: Pressing; Green strength; Clays

1. Introduction

Green mechanical strength is a key property in green pressed bodies, since it is essential these compacts should be able to withstand, without damage, the thermal and mechanical stresses they undergo during the pre-firing stages. In addition to green handling considerations, green strength can be indicative of how well a ceramic processing system is working [1–3]. Defects originating in the earliest processing stages have been shown to persist into the final product [4,5]. Current product losses from cracking and breakage of green tiles are estimated at 3%, while fired product losses from cracks in green tiles are estimated at about 2%. This means that in Europe alone, every year, the losses associated with tile cracks and breakage amount to about 200 million euros, in addition to some 625 000 tons of solid wastes that mainly go to landfills. Powder compact strength is also of interest from a scientific viewpoint, since it provides information on the packing structure and particle interaction forces. The strength of green bodies has thus been the subject of numerous studies. In order appropriately to explain a material's mechanical behaviour during fracture and to attempt to relate a material's mechanical strength to its microstructural characteristics, or to try to explain the role of ceramic processing in mechanical strength, it has often been necessary to use fracture theories such as Linear Elastic Fracture Mechanics (LEFM). Indeed once tensile strength, σ_f, and fracture toughness, K_{IC}, have been determined, critical crack size, a, can be calculated using LEFM. This approach is very interesting when the critical crack size can be related to processing conditions or microstructural characteristics. Few attempts have been made, however, to apply LEFM to failure in green bodies. For porous particulate solids with low volume fractions of polymeric binders, Adams et al. [6–8], and later Ennis et al. [9], obtained fracture toughness, K_{IC}^{A}, from the fracture stress of straight-notched bars, σ, by the three-point bend test (single-edge notched beam) SENB, using the following equation:

$$K_{IC}^{A} = Y\sigma(\bar{a})^{1/2} \quad (1)$$

where $\bar{a}$ is effective crack length and Y is a function of $\bar{a}$, the geometry and loading of the body [10]. The value of $\bar{a}$ is

* Corresponding author.
E-mail address: vicente.cantavella@itc.uji.es (V. Cantavella).

0955-2219/$ – see front matter © 2008 Elsevier Ltd. All rights reserved.
doi:10.1016/j.jeurceramsoc.2008.05.004

given by the sum of notch depth a_0, and a quantity a', obtained together with K_{IC}^{A} by fitting the pairs of values (σ, a_0) to the equation:

$$K_{IC}^{A} = Y\sigma(a_0 + a')^{1/2} \quad (2)$$

For these researchers critical crack size, a', does not represent a natural flaw size but a process zone ahead of the crack tip where microcracking occurs, since critical crack size, which is several times larger than particle size, is not sensitive to binder composition, porosity, or particle size.

Bortzmeyer et al. [11] determined the fracture toughness of a green zirconia body, also using three-point bend bars with a straight notch (SENB). To calculate fracture toughness, K_{IC}^{B}, they applied Eq. (2), assuming that notch depth, a_0, practically coincided with effective crack length, $\bar{a}$. This is an acceptable assumption when the critical crack size, a', is much smaller than a_0.

Bortzmeyer calculated critical crack size, according to the most common procedure, from bending strength, σ_f, and the value of K_{IC}^{B}, from the following equation:

$$a = \left(\frac{K_{IC}}{Y\sigma_f}\right)^2 \quad (3)$$

The critical crack size, a (about 200 μm) calculated in this fashion was much larger than the maximum pore size (about 0.2 μm), determined by mercury porosimetry, and depended on forming conditions. Thus, critical crack size, a, decreased as pressed compact density increased.

Lan et al. [12] determined the fracture toughness of spray-dried alumina powder compacts from the fracture work per unit cross-sectional area, G_C, and the elastic modulus, E, using the equation derived by Irwin:

$$K_{IC}^{I} = (EG_C)^{1/2} \quad (4)$$

G_C was obtained by integrating the load–displacement curve of the unnotched bars tested at a very low cross-head displacement rate (≈20 μm min^{-1}), because the fracture behaviour of the green bars at this rate was non-catastrophic. Critical crack size, a, obtained from Eq. (3), was found to be independent of compaction pressure, compact relative density, and granule hardness. In addition, the critical crack size, a (about 300 μm) was five or six times the granule size.

More recently, Zhang and Green [13] and Uppalapati and Green [14] determined the fracture toughness of spray-dried powder compacts by notched diametral compression tests. Surprisingly, the calculated critical crack sizes, a, obtained from Eq. (3), increased with increased compaction stress. Just as the other researchers, they found that the magnitudes of the calculated critical crack sizes were relatively large (about 1 mm), several times the granule size (about 200 μm). It is hypothesised that subcritical crack growth can occur prior to failure at sites where the voids and defects in the compact coalesce, resulting in the large critical crack size. However, the effect of pressing pressure on critical crack size is inexplicable.

The chevron-notched three-point bend test (CNB) is often used to measure the fracture toughness of brittle materials such as ceramics, since it is a relatively simple experimental procedure while, in brittle materials, use of the chevron-notched specimen alleviates the problem of introducing pre-cracks in the sample. In addition, it is possible to calculate fracture toughness without measuring crack length or the load point displacement, using only the maximum load value recorded during the test [15]. In addition, once the continuous load–deflection curves have been obtained, the fracture work can be calculated, since crack extension is always controlled. Chevron-notch geometry presents an increasingly larger crack front to the advancing crack, thus forcing the crack to extend in a stable manner over the complete area of the chevron notch. This requirement cannot be readily achieved by standard three-point beam bending tests (notched or unnotched). Furthermore, with the CNB procedure, fracture toughness is practically independent of notch width [16,17], in contrast to what occurs with the SENB test [11,18].

Despite the advantages of the CNB test, and though it has been considered appropriate for the determination of toughness in highly porous materials, it even being recommended for green bodies [19,20], the test has never been used to characterise spray-dried powder compacts. Similarly, a literature search found no study on the effect of granule size on the fracture properties of green powder compacts, even though this characteristic has a notable effect on green [21–23] and fired [24] mechanical properties. Moreover, an examination of the effect of granule size on green characteristics and properties becomes of even greater interest if it is taken into account that almost all studies are conducted with granules obtained in pilot spray-driers, the granules thus being smaller than those produced on an industrial scale. This study has sought, first, to apply LEFM to the failure of spray-dried pressed compacts, and to determine the effect of granule size on body fracture properties and the relation between these properties and the microstructural characteristics of the pieces. Secondly, a comparative study has been conducted of the three-point bend test with straight-notched bars (SENB), the most widely used procedure, and the chevron-notched three-point bend test (CNB), with a view to using the latter in subsequent studies.

2. Experimental

2.1. Materials and slurry preparation

Slurries of stoneware floor tile compositions were obtained [21]. They were prepared in industrial discontinuous ball mills (SACMI MTD 380) by mixing red clays, wastewater, and deflocculant (tripolyphosphate–metasilicate 3:1 in weight). The water used was very hard; its specific electrical conductivity was 1980 μS/cm. In order to select the optimum solids and deflocculant content, flow curves were determined using a Bolin CS-50 rheometer. The flow curves of slurries with the optimum deflocculant content (0.75 wt%) and different volume fraction (φ) are shown as examples in Fig. 1.

In order to attempt to relate resulting granule characteristics, such as morphology and porosity, to the rheological behaviour of the slurries [25], the flow curves were fitted to the Casson equation

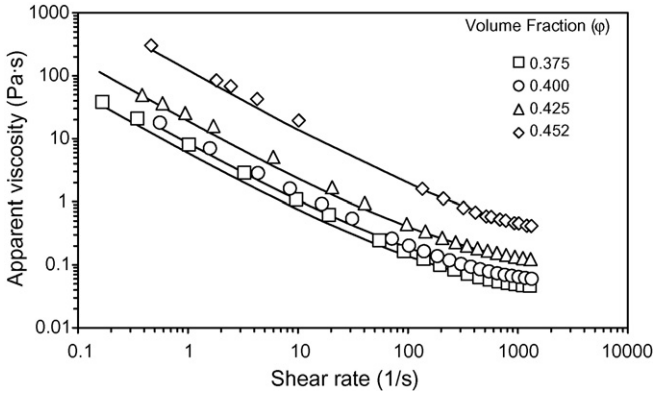

Fig. 1. Influence of volume fraction, φ, on the slurry flow curve. The data have been fitted to the Casson model, Eq. (5).

[26]:

$$\tau^{0.5} = \tau_y^{0.5} + \eta_\infty \dot{\gamma}^{0.5} \quad (5)$$

where τ is the shear stress, τ_y the apparent yield stress, $\dot{\gamma}$ the shear rate, and η_∞ a viscosity limit for infinite shear rate.

The values of τ_y and η_∞ for these suspensions have been plotted in Fig. 2. Both are observed to increase with φ, the effect of φ on τ_y being very pronounced for values of $\varphi \geq 0.425$. Since appropriate slurry discharge from industrial discontinuous mills requires that slurry rheological behaviour at low shear rates should be characterised by low apparent yield stress (τ_y), in view of the results of Fig. 2, a volume fraction of $\varphi \approx 0.40$ was selected as optimum solids content. The particle size distribution of the milled powder, measured by X-ray scattering, Sedigraph, is plotted in Fig. 3.

2.2. Spray drying and powder characterisation

An industrial spray drier (SACMI ATM 110) was used to obtain ceramic granules. The spray drier is classified as a mixed flow spray drier, based on the directions of air and product flow through the drying chamber [27]. The atomisers are spray pressure nozzles, through which slurry is pumped at high pressure. The spray nozzles are mounted on a series of radially arranged lances in the middle of the chamber, hot air being fed into the top

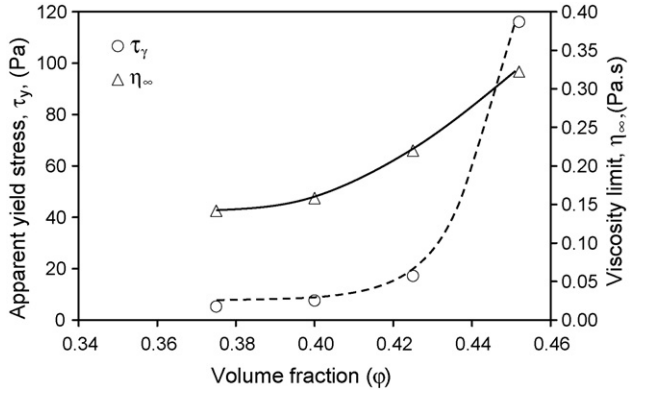

Fig. 2. Influence of volume fraction, φ, on τ_y and η_∞ of the Casson model, Eq. (5).

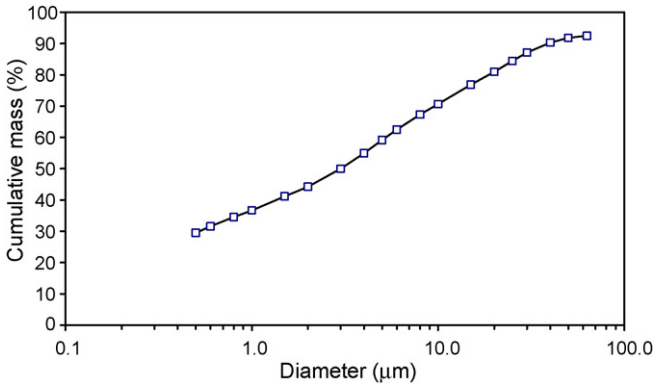

Fig. 3. Slurry particle size distribution.

of the chamber. The maximum water evaporation capacity is 11 000 kg/h. The tower inlet temperature was about 550 °C and the exhaust air temperature was above 100 °C.

The granule size distribution of the resulting powder, SD, was log normal with a geometric median diameter of 345 μm and geometric standard deviation of 230 μm. The SD powder was separated by hand sieving into two granule size fractions: coarse (400–500 μm), C, and fine (100–200 μm), F. The pore size distribution in the granules was determined by mercury intrusion porosimetry.

Granules were also examined using electron microscopy. The relative volume of the single large internal cavity present in the hollow granules was determined for the F and C powders using standard quantitative stereological methods on polished cross-sections of the granule samples mounted in epoxy [25]. At least 130 cross-sections were counted for each fraction.

Prior to compaction, the moisture content of the three powders was adjusted to 0.05 kg water/kg dry solid, and the powders obtained were stored for at least 72 h. Compaction curves were prepared by compacting 20 g samples of the three spray-dried powders at a rate of 1 mm/min in a cylindrical steel die, 40 mm in diameter, using a universal testing machine. Load and displacement were automatically recorded up to a maximum pressure of 40 MPa. Once the final dimensions of the resulting compact had been determined, the log pressure–compactness

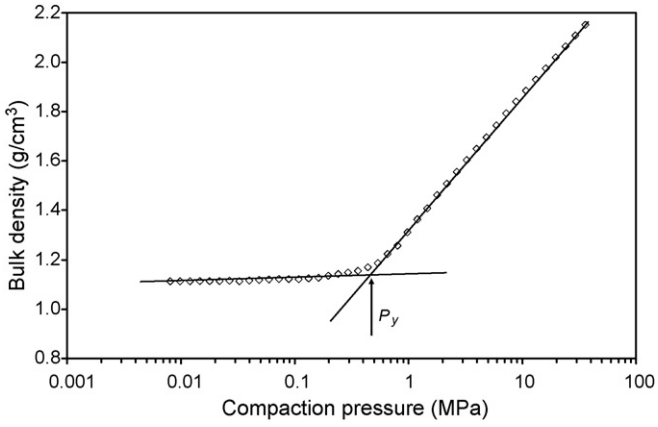

Fig. 4. Compaction curve of the fine fraction, F. Determination of apparent yield pressure, P_y.

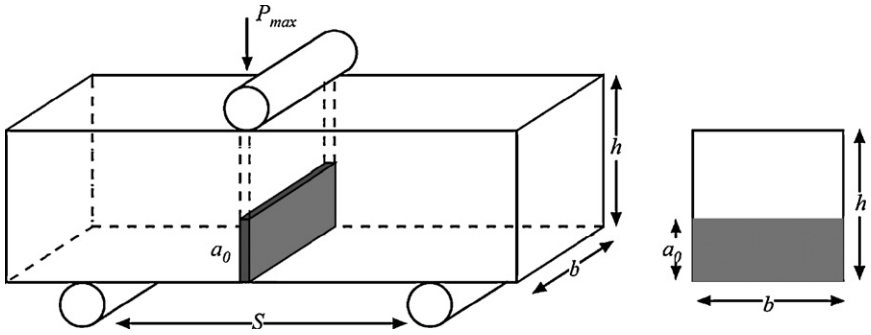

Fig. 5. Single-edge notched three-point bend specimen.

response (compaction diagram) could be back-calculated from the load–displacement curves. Corrections for springback and the deformation were made, as described by Mort et al. [28]. The apparent yield pressure, P_y, was determined from the intersection of two straight lines fitted to the low-pressure and high-pressure legs of the compaction diagram [29–32] (Fig. 4). Apparent yield pressure, P_y, is believed to be a measure of the granule strength [29,30,33]. Five experiments were conducted for each powder.

In order directly to measure granule mechanical strength, σ_{fG}, at least 15 individual granules were tested by subjecting them to compression stress, recording the force with a 10 N Instron load cell. Mechanical strength, σ_{fG}, was calculated from the equation [34]:

$$\sigma_{fG} = \frac{2.8F_{fG}}{\pi D_G^2} \quad (6)$$

where D_G is granule diameter and F_{fG} the breaking load.

2.3. Pressing and characterisation of the bars

Bars for mechanical testing were formed by pressing each powder in a 80 mm × 20 mm rectangular steel die in a hydraulic laboratory press, using a maximum pressure of 30 MPa and powder moisture content of 0.05 kg water/kg dry solid (industrial pressing conditions). The resulting bars were then dried at 110 °C for 3 h. Bulk density of the dry bars was determined by mercury displacement [35] and bar pore diameter distribution was determined by mercury intrusion porosimetry.

Surface topography profiles of the dried compacts were obtained by a non-contacting laser profilometer. Surface profile roughness was quantified by calculating the average roughness, R_a, and root mean square profile height, R_q [36,37]. The surface area above any valley depth was calculated from the digitised surface profile. This bearing–area curve is also called the Abbott curve[38].

In order to determine test bar flexural strength, σ_f, and Young's modulus, E, the 80 mm × 20 mm × 7 mm bars were broken in three-point bending. The distance between two roller supports was $S = 60$ mm. Cross-head speed during all mechanical testing was 1 mm/min.

The following tests were used to determine fracture toughness and fracture work:

i) Single-edge notched beam test (SENB).

The test specimen was a bar of length $L = 80$ mm, width $b = 20$ mm, and thickness $h = 12$ mm. A number of notches, 0.3 mm wide and of different depth, $a_0 < 8$ mm, were made in the centre of the bar by abrasive cutting with wheels. The bar was positioned centrally on two roller supports a distance $S = 60$ mm apart with the notch on the underside (Fig. 5). Fracture toughness was calculated according to the Adams et al. [6–8], and Bortzmeyer et al. [11] methods, indicated above. The method of calculating fracture work per unit cross-sectional area, G_C^A, depended on crack stability, which was governed for these materials by notch depth, a_0. For stable fracture, according to Adams et al. [6–8]:

$$G_C^A = \frac{U}{b(h - \bar{a})} \quad (7)$$

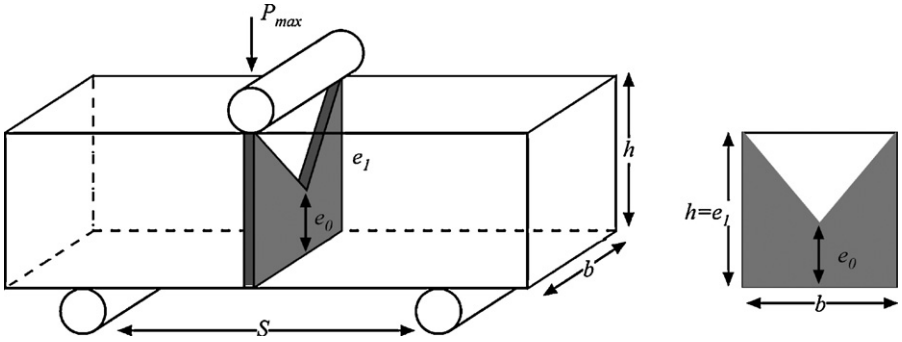

Fig. 6. Chevron-notched three-point bend specimen.

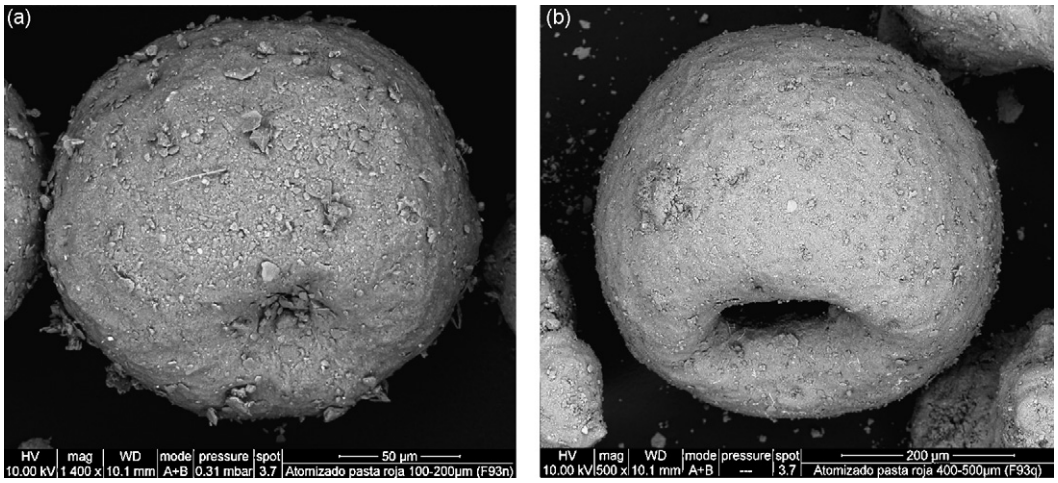

Fig. 7. Typical granules used to prepare specimens for mechanical testing: (a) fine granule, F and (b) coarse granule, C.

where U is fracture work, obtained by integrating the load–displacement curve.

ii) Chevron-notched three-point bend test (CNB).

The test specimen was a bar of 80 mm × 20 mm × 12 mm with a chevron notch (Fig. 6), known as the Tattersall–Tappin specimen configuration. The characteristic dimensions of the notch are: $\alpha_1 = e_1/h = 1$ and $\alpha_0 = e_0/h = 0.2$, the value $\alpha_1 = 1$ being preferred [39].

Fracture toughness, K_{IC}^{C}, was calculated as follows:

$$K_{IC}^{C} = \frac{P_{max}}{bh^{1/2}} Y_{min} \quad (8)$$

where P_{max} is the maximum fracture load, and Y_{min} the minimum geometry correction factor, which depends on the dimensions of the notched specimen.[40]

The fracture work per unit cross-sectional area, G_C^C, was calculated from the following equation:[40]

$$G_C^C = \frac{U}{bh[1 - 1/2(\alpha_1 + \alpha_0)]} \quad (9)$$

3. Results and discussion

3.1. Granule characteristics

Fig. 7 shows typical granules that were used in this study. Granule characteristics are listed in Table 1. The uncertainty corresponds to a 95% statistical confidence level. The granules were hollow, roughly spherical, and contained a single large spherical cavity connected to the external surface by a single large channel. This result is consistent with the mechanism proposed for spray drying a deflocculated slurry.[25,27] It is believed that clay particles, at a low slurry apparent yield stress, are drawn to the droplet surface with the capillarly induced moisture flow to form a rigid shell. A partial vacuum forms inside the droplet, so that the granules collapse near the end of the drying process. In contrast, when the slurry yield stress is sufficiently high to immobilise the particles against the drag force from the migrating water, solid granules are formed.

Polished cross-sections of a coarse granule, C, and fine granule, F, are shown in Fig. 8. The coarse granules displayed the highest ratio of large internal cavity size to granule size. This finding is consistent with the volume fraction values of the large voids of the granules, determined by quantitative stereology (Table 1).

The intragranular porosity distribution curves (interstitial voids in the granule primary particle packing) for the C, F, and SD powders were identical (Fig. 9). Pores larger than 10 μm were found in the pore size distribution in packed beds of F and C spray-dried granules before pressing. However, they were assumed to correspond to the space between granules and were omitted in this figure, which shows that the most frequent pore size (about 0.30 μm) is about 10 times smaller that the average particle size (about 3 μm, Fig. 3). This result is consistent with the observed granule morphology and the rheological characteristics of the slurry, so that dense particle packing results from the dispersed slurry.

As may be observed in Fig. 9, the pore size distributions of the F and C spray-dried granules after pressing at 30 MPa are

Table 1
Granule characteristics

Powder	Intragranular pore volume (cm^3/g)	Volume fraction of large voids in granules	Apparent yield pressure, P_y (MPa)	Granule mechanical strength, σ_{fG} (MPa)
SD	0.197 ± 0.002	–	0.44 ± 0.03	–
F	0.196 ± 0.002	0.065 ± 0.016	0.48 ± 0.04	1.38 ± 0.18
C	0.197 ± 0.002	0.107 ± 0.021	0.28 ± 0.02	0.64 ± 0.15

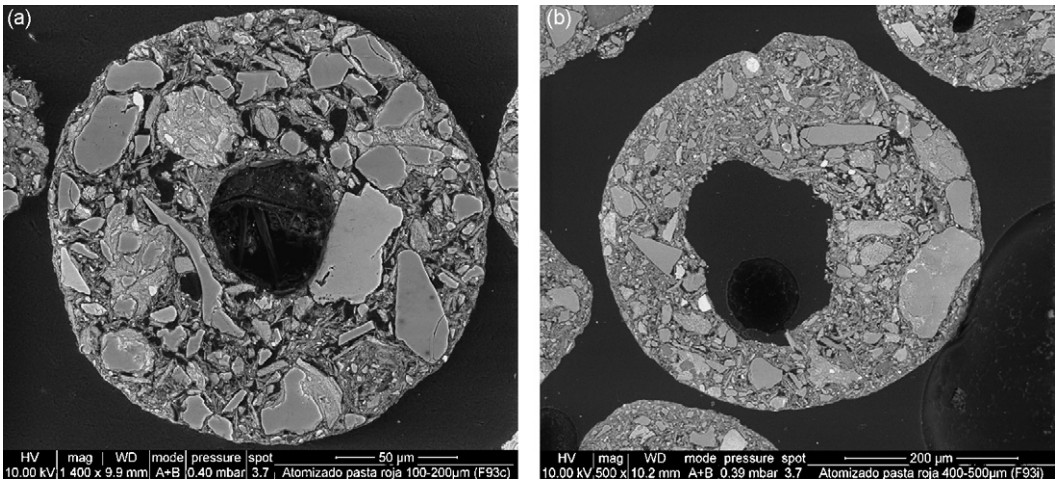

Fig. 8. Polished cross-sections showing the internal structure of typical granules: (a) fine granule, F and (b) coarse granule, C.

monomodal (intergranular pores are not detected) and there are no differences between the curves corresponding to the F and C sets of bars. Table 1 shows further that apparent yield pressure of the powder increases as average granule size decreases, especially when the F and C powders are compared. This behaviour, commonly observed in spray-dried powders [41–43], basically occurs here because increased granule size is accompanied by a considerable increase in the relative size of the single large internal cavity.

Table 1 also gives granule mechanical strength, calculated from Eq. (6). This equation assumes that the granule is homogeneous and solid, and that fracture starts at the granule centre [44], which is not true for the granules used. This equation is customarily used, nonetheless, to characterise granules mechanically, whether the granules are hollow or solid. In the studied case, when granule diameter increases, centre cavity size increases more markedly, which might explain the difference in mechanical strength between the F and C fractions.

Comparison of the values of σ_{fG} and P_f shows that both follow the same trend when granule size is varied.

3.2. Mechanical strength and Young's modulus

The mechanical strength, σ_f, and Young's modulus, E, of the test bars made under standard pressing conditions from the as-received spray-dried powder, SD, its coarse fraction, C, and fine fraction, F, are detailed in Table 2. Twelve bars were tested for each powder. The table includes the average compactness values, ϕ, of the test bars. It shows that, at the forming values used (pressing pressure = 30 MPa and pressing moisture = 0.05 kg water/kg dry solid), bar compactness, ϕ, and pore size distribution (Fig. 9) are practically independent of granule size [31,43]. Only small differences are to be observed between the values of ϕ corresponding to the F and C series. The same applies to the elastic modulus, E. In contrast, the effect of average granule size on bar strength is significant as already observed in other studies.[21,22]

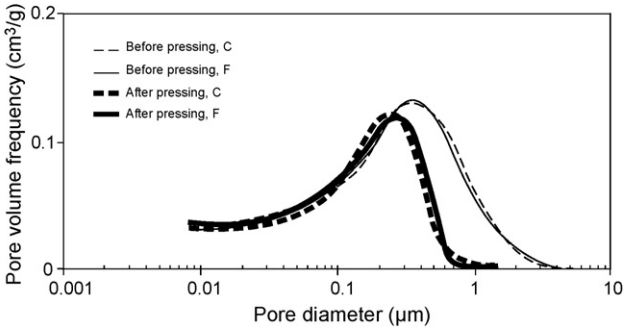

Fig. 9. Intragranular pore size distribution in packed beds of spray-dried granules before pressing and after pressing at 30 MPa, for fine granules, F, and coarse granules, C.

3.3. Fracture toughness

To illustrate the problems of applying a simple linear analysis like that of Bortzmeyer et al. [11], Fig. 10 displays a plot of K_{IC}^{B} as a function of a_0/h for the three sets of bars, calculated from Eq. (2), assuming that $\bar{a} = a_0$; i.e. notch depth, a_0, coincides with effective crack length, $\bar{a}$. It shows, as noted in the introduction, that for high a_0/h values, the values of K_{IC}^{B} are independent of this ratio. In contrast, for low a_0/h values, the values of K_{IC}^{B} decrease as a_0/h decreases, this effect being greater as average granule size increases. It also shows that the value of a_0/h beyond which K_{IC}^{B} no longer depends on this parameter increases with granule size. Both facts suggest that critical crack size, a', increases with average granule size. In addition, the average toughness value, K_{IC}^{B}, is observed to depend very little on granule size (Fig. 10, Table 3). Indeed, the differences between the average values of

Table 2
Compactness, ϕ, mechanical strength, σ_f, and Young's modulus, E, of the sets of bars made from the as-received spray-dried powder, SD, coarse powder fraction, C, and fine powder fraction, F

Set	ϕ	σ_f (MPa)	E (GPa)
SD	$0.7381 \pm 6 \times 10^{-4}$	3.33 ± 0.05	3.32 ± 0.04
F	$0.7370 \pm 1 \times 10^{-3}$	3.56 ± 0.07	3.20 ± 0.06
C	$0.7423 \pm 5 \times 10^{-4}$	3.07 ± 0.07	3.44 ± 0.07

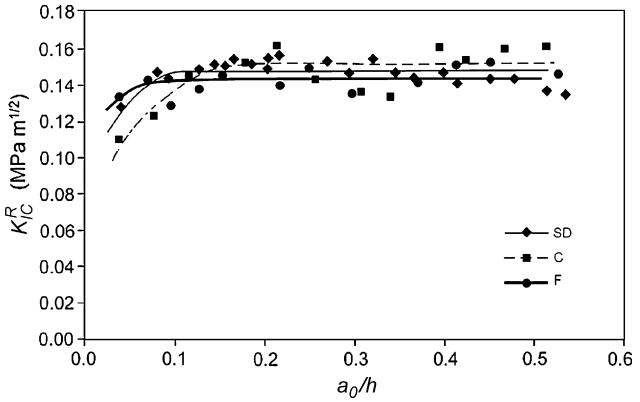

Fig. 10. Plots of K_{IC}^{B}, as a function of a_0/h, calculated from Eq. (2) for the SD, C, and F sets of bars.

Table 3
Fracture toughness values of the SD, C, and F sets of bars, obtained using different procedures

Set	K_{IC}^{B} (MPa m$^{1/2}$)	K_{IC}^{A} (MPa m$^{1/2}$)	K_{IC}^{C} (MPa m$^{1/2}$)
SD	0.147 ± 0.003	0.175 ± 0.005	0.168 ± 0.004
F	0.142 ± 0.004	0.160 ± 0.002	0.159 ± 0.004
C	0.150 ± 0.008	0.180 ± 0.007	0.175 ± 0.003

K_{IC}^{B} for each series are of very little significance, since they are smaller than the measurement scatter. In view of the results of Fig. 10, the procedure used by Adams,[6–8] for the simultaneous calculation of K_{IC}^{A} and a' was applied. According to this author, when the values of the fracture stress of notched bars, σ, are initially plotted versus $1/(Y\sqrt{a_0 + a'})$, for values of $a' = 0$, the curved line shown in Fig. 11 is obtained. Values of a' are then judiciously introduced until, by means of an iterative process, the optimal value of a' is obtained which linearises the foregoing curve (Fig. 11). The slope of this straight line is K_{IC}^{A}. Table 3 presents the values of K_{IC}^{A} and Table 5 details the values of a' obtained by this method for the three series.

The results of the chevron-notched three-point bend test, K_{IC}^{C}, for the three sets, which each comprised 12 bars, are given in Table 3. The results indicate that the values of K_{IC}^{A} and K_{IC}^{C}

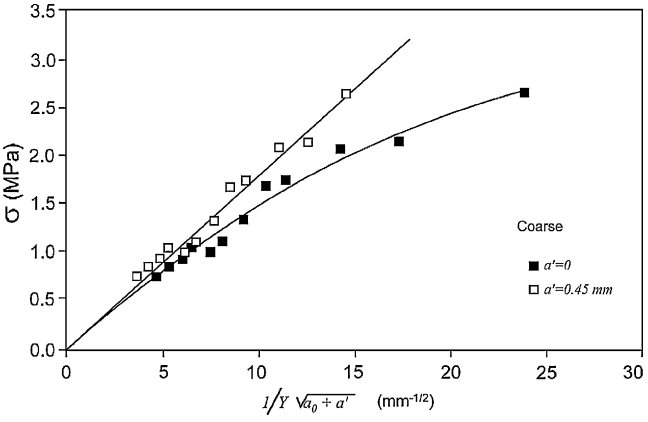

Fig. 11. Plots of σ as a function of $1/Y\sqrt{a_0 + a'}$ from notched bars prepared with coarse granules, C.

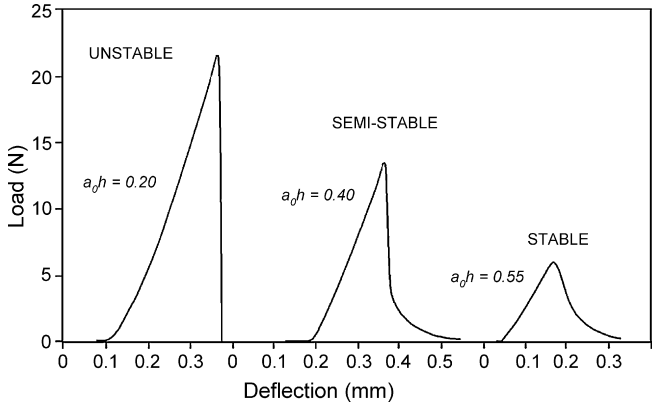

Fig. 12. Experimental load–deflection curves for SENB specimens of the standard set, SD.

corresponding to each series practically coincide and are slightly higher than those obtained by the Bortzmeyer procedure, K_{IC}^{B}, which assumes a' to be negligible in the toughness calculation. Furthermore, a slight dependence may be observed of K_{IC}^{A} and K_{IC}^{C} on average granule size, especially when the results of the extreme series F and C are compared. The fact that the elastic modulus, E, follows the same trend as K_{IC}^{A} and K_{IC}^{C} for the F and C series, to which also extreme values of P_f and σ_{fG} correspond, suggests a slight influence of granule hardness or deformability on these mechanical properties.

3.4. Fracture work G_C^A and G_C^C

The method of calculating G_C^A, using the single-edge notched beam test, depends on crack stability. Each set of bars exhibited a range of fracture stabilities depending on notch size, a_0. Usually only the bars with the highest notch depths displayed fully stable fracture in the three sets. Typical force–deflection curves for notched bars, displaying increased fracture stability with increasing notch depth, are shown in Fig. 12 for the standard set, SD. This behaviour is analogous to that found by Adams [6]. Fig. 13 presents the plot for the standard set, SD, of the values of G_C^A calculated from Eq. (7), considering the following two cases: $\bar{a} = a_0$ and $\bar{a} = a_0 + a'$, where $a' = 0.45$ mm, the value obtained for this series by the Adams procedure. In both cases, the values

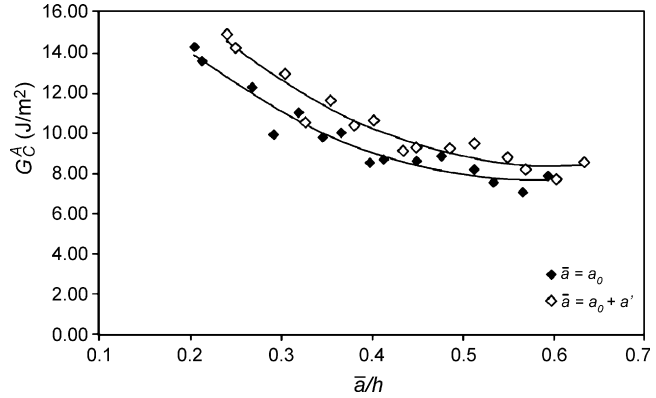

Fig. 13. Variation of G_C^A with $\bar{a}/h$, for the SD set, considering: (i) $\bar{a} = a_0$ and (ii) $\bar{a} = a_0 + a'$, where $a' = 0.45$ mm.

Table 4
Fracture work, G_C^A and G_C^C, and fracture toughness values $(K_{IC}^I)^A$ and $(K_{IC}^I)^C$, calculated from Eq. (4), for the SD, C, and F sets of bars

Set	G_C^A (J/m^2)	$(K_{IC}^I)^A$ (MPa m$^{1/2}$)	$(G_C^C)^A$ (J/m^2)	$(K_{IC}^I)^C$ (MPa m$^{1/2}$)
SD	8.28 ± 0.73	0.166 ± 0.007	8.67 ± 0.20	0.170 ± 0.002
F	8.35 ± 0.56	0.163 ± 0.009	8.54 ± 0.17	0.165 ± 0.002
C	9.30 ± 0.84	0.179 ± 0.011	9.72 ± 0.26	0.183 ± 0.003

Table 5
Critical crack size calculated from Eq. (2), a', and critical crack size calculated from Eq. (3), a, of the values (K_{IC}^C), $a(K_{IC}^C)$, and (K_{IC}^B), $a(K_{IC}^B)$

Set	a' (mm)	$a(K_{IC}^B)$ (mm)	$a(K_{IC}^C)$ (mm)
SD	0.45 ± 0.05	0.65 ± 0.03	0.68 ± 0.03
F	0.35 ± 0.05	0.55 ± 0.03	0.56 ± 0.02
C	0.95 ± 0.07	0.89 ± 0.06	0.92 ± 0.05

of G_C^A decrease as fracture stability increases ($\bar{a}/h$ increases) until reaching a practically constant value for the largest $\bar{a}/h$ values, corresponding to a completely stable fracture. In addition, when the value $a' = 0.45$ mm is considered in the fracture work calculation, the calculated values of G_C^A are a little higher. The other series behave similarly to the analysed series. The values of G_C^A corresponding to each series are detailed in Table 4. Each value of G_C^A is the average of the bars with the highest $\bar{a}/h$ values (4 or 5 specimens), for which G_C^A moves around an average value.

Unlike the SENB test, crack extension is always controlled (stable fracture) in the CNB test, as Fig. 14 shows. The values of G_C^C were calculated from Eq. (9) for the three sets. The results are given in Table 4. Comparison of the values of G_C^C with those of G_C^A shows that the average fracture work values obtained by the CNB test, G_C^C, are slightly higher than those obtained by the SENB test, G_C^A, though the differences cannot be considered significant, since they are smaller than the measurement scatter in the SENB test. Furthermore, the measurement scatter corresponding to the CNB test is observed to be much smaller than that of the SENB test. In addition, comparison of the F and C series results shows that the values of G_C, just like those of K_{IC} and E, increase slightly with average granule size, probably because of the greater compactness of the bars obtained with the coarsest granules as a result of greater granule deformability.

The values of K_{IC}^I have been calculated from the values of Young's modulus, E (Table 2) and G_C^A and G_C^C (Table 4), using Eq. (4). The results are given in Table 4. Comparison of the values of $(K_{IC}^I)^A$ and $(K_{IC}^I)^C$ calculated from Eq. (4) (Table 4) with the experimentally determined values, K_{IC}^B, K_{IC}^A, and K_{IC}^C

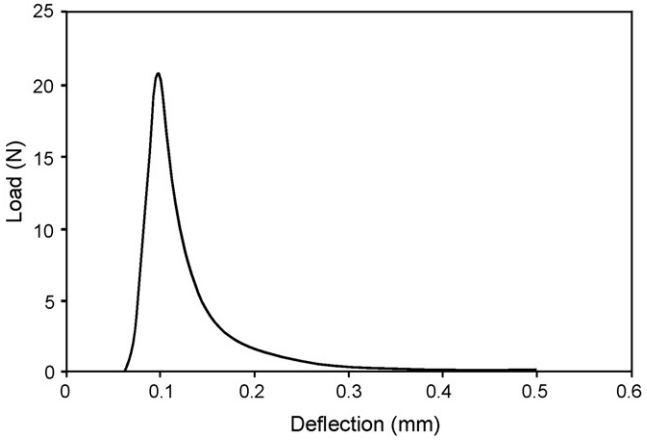

Fig. 14. Experimental load–deflection curve for a CNB specimen of the standard set, SD.

(Table 3) shows that, with the exception of the values of K_{IC}^B (obtained according to the Bortzmeyer procedure), the other procedures yield very similar toughness values for each series. In regard to the measurement scatter, however, the results obtained for $(K_{IC}^I)^A$ from G_C^A, applying the Irwin equation, are clearly unfavourable.

3.5. Critical crack size, a', and a. Relation to the textural characteristics of the piece

Table 5 gives the values of critical crack size, a', calculated by the Adams procedure, Eq. (2), and the values of critical crack size, a, calculated from Eq. (3), using the fracture toughness values obtained according to the Bortzmeyer procedure, $a(K_{IC}^B)$, or those obtained by the CNB test, $a(K_{IC}^C)$. Although there is a certain difference between the values obtained by the different procedures, the values of a' and a increase monotonically with average granule size. In addition, critical crack size, whether calculated as a' or a, was about twice the granule size, in contrast to the results obtained by other researchers, who reported much higher values for this relation[6–9,11–14]. The marked effect of granule size on critical crack size and, hence, on bar mechanical strength, σ_f (since the effect of granule size on toughness is small) may be expected to manifest itself in certain textural or microstructural, surface and/or internal characteristics of the compact in relation to original granule size. The external and fracture surfaces of the F and C sets of bars were therefore observed, first, by SEM (Fig. 15). The external surface of these pieces was then characterised, quantitatively determining the surface topography (Fig. 16) with a non-contacting laser profilometer. The bearing–area curves were also used to quantify the surface topography (Fig. 17a). In this figure the depth of the valleys in the surface profile has been plotted versus the surface above a given depth, expressed as a percentage. The graph shows that valley depth, which is proportional to the size of the intergranular voids, is smaller for the F compact than the C compact, since the bearing–area curve of the F compact lies above that of the C compact. Analogously, the valley depth distribution curve of the C compact surface profile is shifted to notably larger values than the corresponding F compact curve (Fig. 17b). In addition, the values of the surface density of deep valleys (above 10 μm), of average roughness, R_a, and root mean square profile height, R_q, corresponding to the F compact are significantly smaller than those of the C compact (Table 6). In contrast, the total surface density of valleys is greater for the F compact, since the surface density of intergranular voids increases as granule size decreases (Fig. 15a and b).

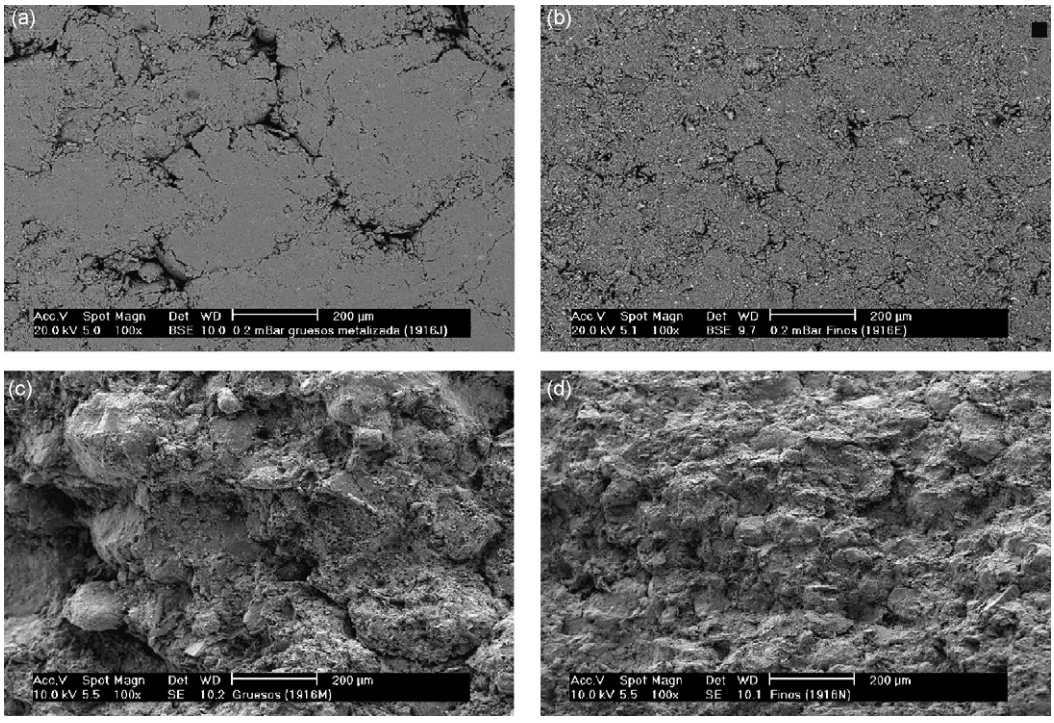

Fig. 15. SEM micrographs of pressed surfaces and fracture surfaces of C (a and c) and F (b and d) bars.

These findings clearly evidence notable textural and microstructural differences between the F and C compacts, both at the surface and inside the pieces. The differences are caused by the persistence of distinct granules, under the typical forming conditions used in industrial practice: though intergranular porosity is no longer detected by mercury porosimetry (Fig. 9), the boundaries between the granules and the porous areas around the granules remain clearly visible, especially at the compact surface (Fig. 15a and b). Indeed, these surfaces are a result of the pressing action of the punch face against the top surface of the

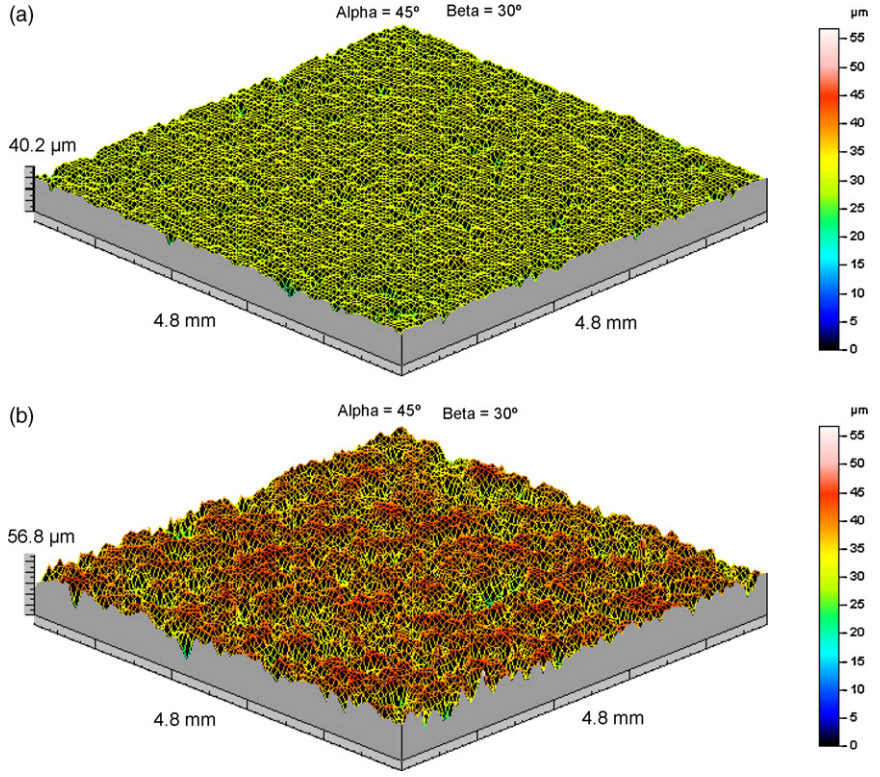

Fig. 16. Topographic profilometer images of test bar surfaces: (a) fine compact, F and (b) coarse compact, C.

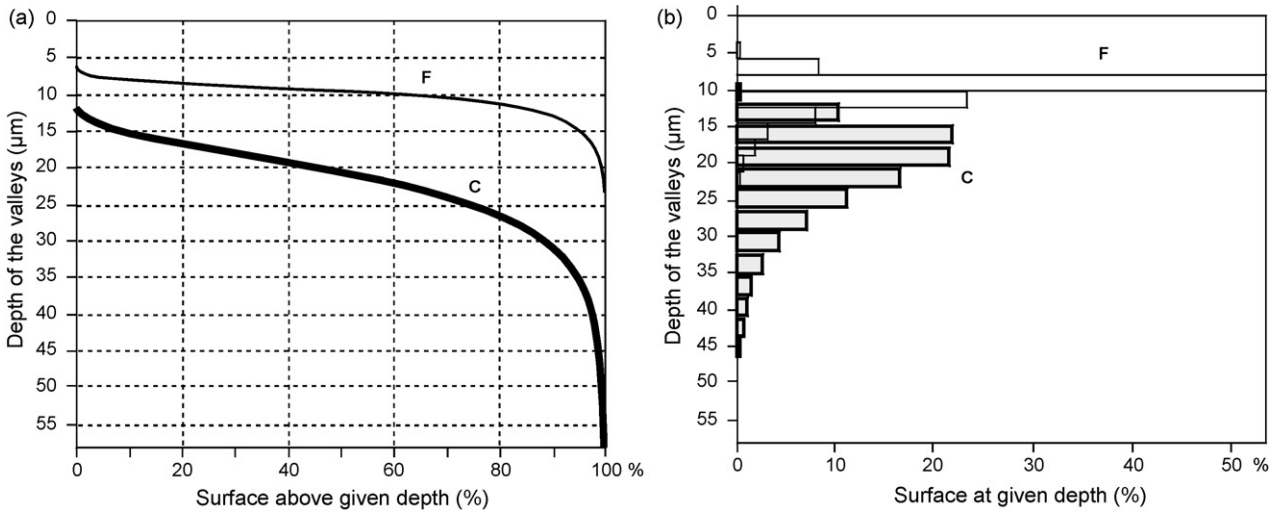

Fig. 17. (a) Bearing–area curves for F and C compacts. (b) Valley depth distribution for F and C compacts.

Table 6
Summary of the topographic results for the F and C compacts

Set	Surface density of deep valleys (>10 μm) (no. of valleys/mm^2)	Total surface density of valleys (no. of valleys/mm^2)	R_a (μm)	R_q (μm)
F	3.2 ± 0.2	210 ± 20	1.4 ± 0.2	2.0 ± 0.4
C	4.4 ± 0.2	180 ± 15	3.5 ± 0.4	4.6 ± 0.5

powder in the die. Friction between the powder and punch may slightly exaggerate the number of defects compared with the interior of the compacts. Nevertheless, the pressed surface still provides a good indication of the large intergranular pores and granule boundaries [29]. Two typical defects are clearly visible in Fig. 15a and b: large intergranular pores and granule interfaces between two compacting granules, defect size obviously depending on granule size.

Although these micrographs (Fig. 15a and b) apparently display many large pores in the green bodies, Fig. 9 shows that the large pores are not determined by mercury porosimetry. This seemingly conflicting outcome occurs because the volume fraction of the void space around the unfractured granules becomes negligibly small compared with the total volume fraction of pores.

In addition, the typical fracture surfaces of spray-dried compacts C and F exhibit a mixture of transgranular and intergranular failure, since there are still granules left whose contacts with other granules are weak (intergranular failure); however, most such contacts are strong, since few granules are distinguished at the compact fracture surface (transgranular failure) (Fig. 15c and d). Since crack paths follow the weakest links (namely, intergranular boundaries or voids), cracks may be expected to originate at these defects, flaw size being very similar to original granule size. On the other hand, no significant subcritical crack growth by coalescence of microcracks originating at a defect is needed to reach critical crack size and subsequent fracture in these compacts, because critical crack size is only a little larger than the granules. This last finding contrast to the results reported by other researchers, in which it was found that this fracture mechanism (subcritical crack growth) needed to develop considerably [6–9,12–14]. Although there are important differences between the characteristics of the compacts studied in this paper and those that appear in the literature cited previously (granule size, compact porosity, nature of the material, and particle size distribution), the authors believe that the use of polymer binders in forming the pieces is the most important reason for the pieces to display, during fracture, significant subcritical crack growth or a process zone ahead of the crack tip. Spray-dried compacts thus exhibit viscoelastic properties [14], unlike those obtained in this study, which had no organic binders and were dry, and therefore displayed much more elastic behaviour [21]. The viscoelastic behaviour noted may be attributed to the ductibility of the organic binder, which is moreover highly dependent on relative humidity. Therefore, bonds between particles can undergo larger shear displacement before failure, thus resulting in increased failure strength and non-linear behaviour of the load–displacement curve. In addition, at 50% relative humidity (ambient conditions), at which many mechanical strength tests are conducted, the ductibility of the organic binder and the compact is high.

4. Conclusions

The following conclusions may be drawn from the study:

- Under optimum rheological conditions of the slurry, i.e. maximum solids content ($\varphi = 0.40$) compatible with low apparent yield stress ($\tau_y \leq 10$ Pa), the granules obtained by spray drying were hollow (containing a single large open void or crater) and displayed high particle packing density.

- When the as-received spray-dried powder (SD), the coarse powder fraction, C (400–500 μm) and the fine powder fraction, F (100–200 μm), obtained by hand sieving SD, were characterised, the relative volume of the single large internal cavity was observed to be notably larger in the coarser granules than in the finer ones. The remaining studied morphological and structural characteristics did not alter with granule size.
- The apparent yield pressure, P_y, and the granule strength, σ_{fG}, of the C fraction was much smaller than those of the F fraction, owing to the smaller relative volume of the large internal cavity of the latter.
- Fracture toughness, determined by the SENB method, depended on the relative depth of the notch when the notch was small. In addition, this dependence was a function of granule size. Such behaviour may be explained by considering the existence of a crack or process area whose size is not negligible in relation to that of the notch.
- The fracture toughness values obtained by the SENB method, considering a non-negligible crack length in relation to the notch, were very similar to those obtained by the chevron-notched beam (CNB) procedure, which does not require specification of a crack length in order to calculate toughness, and is not as sensitive as the SENB method to notch width.
- As the relative depth of the notch increased in the SENB test, fracture became more stable. For sufficiently deep notches, the energy obtained approached that determined by the CNB test, in which fracture was always stable. The measurement scatter found with the CNB method was smaller than that found with the SENB method.
- The values of K_{IC}, G_C, and E increased slightly with granule size, possibly as a result of the greater deformability and lower strength of the coarse granules.
- Crack size or process zone length increased with granule size. In addition, the value determined for this length was twice the size of the granule, unlike the results obtained by other researchers, who report much larger crack lengths.
- Compact topography, with the determination of the surface density of the deep valleys and surface roughness of test bars prepared from either fine or coarse granules, displayed significant differences, which were correlatable to the crack length values obtained from LEFM. In addition, these defects might initiate fracture of the compact, so that coalescence phenomena might have a more limited extension than that suggested by other authors.

References

1. Carneim, T. J. and Green, D. J., Mechanical properties of dry-pressed alumina green bodies. *J. Am. Ceram. Soc.*, 2001, **84**(7), 1405–1410.
2. Kendall, K., Influence of powder structure on processing and properties of advanced ceramics. *Powder Technol.*, 1989, **58**, 151–161.
3. Hsieh, H. and Fang, T., Effect of green states on sintering behavior and microstructural evolution of high-purity barium titanate. *J. Am. Ceram. Soc.*, 1990, **73**(6), 1566–1573.
4. Shinohara, N., Okumiya, M., Hotta, T., Nakahira, K., Naito, M. and Uematsu, K., Formation mechanisms of processing defects and their relevance to the strength in alumina ceramics made by powder compaction process. *J. Mater. Sci.*, 1999, **34**, 4271–4277.
5. Kendall, K., Alford, N. McN. and Birchall, J. D., The strength of green bodies. *Brit. Ceram. Proc.*, 1986, **8**, 255–265.
6. Adams, M. J., The strength of particulate solids. *J. Powder Bulk Solids Technol.*, 1985, **9**, 15–20.
7. Mullier, M. A., Seville, J. P. and Adams, M. J., A fracture mechanics approach to the breakage of particle agglomerates. *Chem. Eng. Sci.*, 1987, **42**, 667–677.
8. Adams, M. J., Williams, D. and Williams, J. G., The use of linear elastic fracture mechanics for particulate solids. *J. Mater. Sci.*, 1989, **24**, 1772–1776.
9. Ennis, B. J. and Sunshine, G., On wear as a mechanism of granule attrition. *Tribol. Int.*, 1993, **26**, 319–327.
10. Rooke, D. P. and Cartwright, D. J., *Compendium of Stress Intensity Factor*. HMSO, London, 1976.
11. Bortzmeyer, D., Langguth, G. and Orange, D., Fracture mechanics of green products. *J. Eur. Ceram. Soc.*, 1993, **11**, 9–16.
12. Lam, D. C. C. and Kusakari, K., Microstructure and mechanical properties relations for green bodies compacted from spray dried granules. *J. Mater. Sci.*, 1995, **30**, 5495–5501.
13. Zhang, Z. and Green, D. J., Fracture toughness of spray-dried powder compacts. *J. Am. Ceram. Soc.*, 2002, **85**, 1330–1332.
14. Uppalapati, M. and Green, D. J., Effect of relative humidity on the viscoelastic and mechanical properties of spray-dried powder compacts. *J. Am. Ceram. Soc.*, 2006, **89**, 1212–1217.
15. Munz, D., Bubsey, R. T. and Shannon Jr., J. L., Fracture toughness determination of Al_2O_3 using four-point-bend specimens with straight-through and chevron notches. *J. Am. Ceram. Soc.*, 1980, **63**, 300–305.
16. Munz, D., Bubsey, R. T. and Shannon Jr., J. L., Performance of chevron-notch short bar specimen in determining the fracture toughness of silicon nitride and aluminum oxide. *J. Test. Eval.*, 1980, **8**, 103–107.
17. Kolhe, R., Hui, C. and Zehnder, A. T., Effects of finite notch width on the fracture of chevron-notched specimens. *Int. J. Fract.*, 1998, **94**, 189–198.
18. Coquard, P. and Boistelle, K., Thermodynamical approach to the brittle fracture of dry plasters. *J. Mater. Sci.*, 1996, **31**, 4573–4580.
19. Ouchiyama, N., Benbow, J. J. and Bridgwater, J., On the fracture toughness of extrudates and its relationship to rates of bulk particle attrition. *Powder Technol.*, 1987, **51**, 103–114.
20. Bika, D. G., Gentzler, M. and Michaels, J. N., Mechanical properties of agglomerates. *Powder Technol.*, 2001, **117**, 98–112.
21. Jarque, J.C., Estudio del comportamiento mecánico de soportes cerámicos crudos. Mejora de sus Propiedades Mecánicas, Ph.D. thesis, Universitat Jaume I de Castelló, Castelló, 2001.
22. Amorós, J. L., Felíu, C. and Agramunt, J. V., Mechanical strength and microstructure of green ceramic bodies. *Ceram. Acta*, 1996, **8**(6), 5–19.
23. Mosser, B. D., Reed, J. S. and Varner, J. R., The effect of granule size on green strength distributions of dry-pressed alumina compacts. In *Ceramic Transactions, Vol. 1, Ceramic Powder Science*, ed. G. L. Messing, E. R. Fuller Jr. and H. Hausneer. American Ceramic Society, Westerville, 1988, pp. 767–775.
24. Mosser, B. D., Reed, J. S. and Varner, J. R., Strength and Weibull modulus of sintered compacts of spray-dried granules. *Ceram. Bull.*, 1992, **71**, 105–109.
25. Walker Jr., W. J. and Reed, J. S., Influence of slurry parameters on the characteristics of spray-dried granules. *J. Am. Ceram. Soc.*, 1999, **82**, 1711–1719.
26. Barnes, H. A., *Viscosity*. Cambrian Printers, Aberystwyth, 2002.
27. Lukasiewicz, S. J., Spray-drying ceramic powders. *J. Am. Ceram. Soc.*, 1989, **72**, 617–624.
28. Mort, P. H., Sabia, R., Niesz, D. E. and Riman, R. E., Automated generation and analysis of powder compaction diagrams. *Powder Technol.*, 1994, **79**, 111–119.
29. Balasubramanian, S., Shanefield, D. J. and Niesz, D. E., Effect of internal lubricants on defects in compacts made from spray-dried powders. *J. Am. Ceram. Soc.*, 2002, **85**, 134–138.
30. Balasubramanian, S., Shanefield, D. J. and Niesz, D. E., Effect of externally applied plasticizer on compaction behavior of spray-dried powders. *J. Am. Ceram. Soc.*, 2002, **85**, 749–754.
31. Amorós, J.L., Orts, M.J., Sanz, V. and Escardino, A., Prensado unidireccional de polvos cerámicos aglomerados por atomización. I. Mecanismo

de compactación, In Ciencia y Tecnología de los Materiales Cerámicos y Vítreos. España'89. Faenza Editrice, Castellón, 1990, pp. 133–137.
32. Walker Jr., W. J. and Reed, J. S., Influence of granule character on strength and Weibull modulus of sintered alumina. *J. Am. Ceram. Soc.*, 1999, **82**, 50–56.
33. Song, J. H. and Evans, J. R., A die pressing test for the estimation of agglomerate strength. *J. Am. Ceram. Soc.*, 1994, **77**, 806–814.
34. Kamiya, H., Isomura, K., Jimbo, G. and Jun-Ichiro, T., Powder processing for the fabrication of Si_3N_4 ceramics. I. Influence of spray-dried granule strength on pore size distribution in green compacts. *J. Am. Ceram. Soc.*, 1995, **78**, 49–57.
35. Amorós, J. L., Blasco, A., Manfredini, T. and Pozzi, P., A new experimental method for measuring apparent density in ceramics: aspects of technique and applications. *Ind. Ceram.*, 1987, **7**(4), 200–204.
36. Miller, L., *Engineering Dimensional Metrology*. Edward Arnold, London, 1960.
37. Hutchings, L. M., *Tribology: Friction and Wear of Engineering Materials*. Edward Arnold, London, 1992.
38. Özkan, N. and Briscoe, B. J., The surface topography of compacted agglomerates; a means to optimize compaction conditions. *Powder Technol.*, 1996, **86**, 201–207.
39. Jenkins, M. G., Kobayashi, A. S., White, K. W. and Bradt, R. C., A 3-D finite element analysis of a chevron-notched, three-point bend fracture specimen for ceramic materials. *Int. J. Fract.*, 1987, **34**, 281–295.
40. He, M. Y. and Evans, A. G., Three-dimensional finite elements analysis of chevron-notched, three-point and four-point bend specimens. In *Fracture Mechanics: 22nd Symposium*, ed. H. A. Ernest, A. Saxena and D. L. McDowell, 1992, pp. 471–484.
41. Messing, G. L. and McCoy, L. G., Microstructural development during compaction of spray-dried granules. *Am. Ceram. Soc. Bull.*, 1980, **59**, 347.
42. Frey, K. G. and Halloran, J. W., Compaction behavior of spray-dried alumina. *J. Am. Ceram. Soc.*, 1984, **67**, 199–203.
43. Amorós, J.L., Orts, M.J., Monfort, E. and Escardino, A., Prensado unidireccional de polvos cerámicos aglomerados por atomización. II. Microestructura de la pieza en Crudo, In Ciencia y Tecnología de los Materiales Cerámicos y Vítreos. España'89. Faenza Editrice, Castellón, 1990, pp. 139–144.
44. Takahashi, H., Shinohara, N., Okumiya, M., Uematsu, K., Jun-Ichiro, T., Iwamoto, Y. and Kamiya, H., Influence of slurry flocculation on the character and compaction of spray-dried silicon nitride granules. *J. Am. Ceram. Soc.*, 1995, **78**, 903–908.